# Development of a piezo stack – laser Doppler vibrometer sensing approach for characterizing shear wave dispersion and local viscoelastic property distributions

Bowen Cai[1], Teng Li[3], Luyu Bo[3], Jiali Li[3],
Rani Sullivan[1], Chuangchuang Sun[1], Wayne Huberty[2], Zhenhua Tian[3, *]

[1] *Department of Aerospace Engineering, Mississippi State University, Mississippi State, MS, 39762, USA*
[2] *Advanced Composites Institute, Mississippi State University, Mississippi State, MS, 39762, USA*
[3] *Department of Mechanical Engineering, Virginia Tech, Blacksburg, VA, 24061, USA*
[*] *Corresponding author: Z.T. tianz@vt.edu*

**Abstract:** Laser Doppler vibrometry and wavefield analysis have recently shown great potential for nondestructive evaluation, structural health monitoring, and studying wave physics. However, there are limited studies on these approaches for viscoelastic soft materials, especially, very few studies on the laser Doppler vibrometer (LDV)-based acquisition of time-space wavefields of dispersive shear waves in viscoelastic materials and the analysis of these wavefields for characterizing shear wave dispersion and evaluating local viscoelastic property distributions. Therefore, this research focuses on developing a piezo stack-LDV system and shear wave time-space wavefield analysis methods for enabling the functions of characterizing the shear wave dispersion and the distributions of local viscoelastic material properties. Our system leverages a piezo stack to generate shear waves in viscoelastic materials and an LDV to acquire time-space wavefields. We introduced space-frequency-wavenumber analysis and least square regression-based dispersion comparison to analyze shear wave time-space wavefields and offer functions including extracting shear wave dispersion relations from wavefields and characterizing the spatial distributions of local wavenumbers and viscoelastic properties (*e.g.*, shear elasticity and viscosity). Proof-of-concept experiments were performed using a synthetic gelatin phantom. The results show that our system can successfully generate shear waves and acquire time-space wavefields. They also prove that our wavefield analysis methods can reveal the shear wave dispersion relation and show the spatial distributions of local wavenumbers and viscoelastic properties. We expect this research to benefit engineering and biomedical research communities and inspire researchers interested in developing shear wave-based technologies for characterizing viscoelastic materials.

**Keywords:** Laser Doppler vibrometer, Wavefield analysis, Frequency-wavenumber analysis, Shear wave, Piezoelectric stack, Material property characterization.

## 1. Introduction

The usage of lasers for noncontact generation and acquisition of elastic waves has been attracting increasing attention in recent years for engineering and biomedical applications such as nondestructive evaluation (NDE) [1–3], structural health monitoring [4–6], and biomedical imaging [7–10]. Based on the thermal elastic effect, a pulsed laser can generate different modes of elastic waves such as pressure waves in bulk solids and symmetric and anti-symmetric Lamb modes in plate-like structures [11–13]. On the other hand, based on the Doppler effect, a laser Doppler vibrometer (LDV) can acquire displacement waveforms $u(t)$ of generated elastic waves at the laser location on the test structure's surface [2,5,11]. By further using high-resolution galvo mirrors to redirect a laser beam or linear motion stages to move the laser source location, the laser spot on the test structure can be gradually moved to perform point-by-point wave sensing and obtain a series of waveforms at predefined scanning points, such as points along a straight line, points on a flat surface, and points on a curved surface [5,14,15]. The fusion of these acquired waveforms can further provide time-space wavefields such as $u(t, x)$ for a line scan, $u(t, x, y)$ for a flat-surface scan, $u(t, x, y, z)$ for a curved-surface scan, and these can be used to visually reveal the propagation of elastic waves and the wave interactions with different material damages such as voids, cracks, corrosion, and delamination [1,15–17]. In addition, compared to piezoelectric transducer-based elastic wave generation and sensing, the laser-based methods offer multiple advantages such as high spatial sensing resolution, high flexibility in moving the excitation and sensing locations, and the ability to generate and receive elastic waves from far distances, for example, > 1 m [18–20].

With the aforementioned wavefield sensing capability and other unique features, more studies are leveraging laser technologies for both fundamental studies on elastic wave propagation and wave-damage interaction in complex structures, as well as application studies on detecting various types of damages such as cracks, delamination, and corrosion for the

safety of aerospace, civil, and nuclear structures[1,3,12,17,21–27]. Ambroziński et al. demonstrated that the scanning points of an LDV could be used to efficiently construct phased arrays with various configurations for detecting defects in plate-like structures [23]. Sampath and Sohn developed a noncontact microcrack detection technique based on laser line arrays [12]. Kudela et al. developed a hybrid system that integrated a piezoelectric transducer and a scanning LDV for acquiring wavefields and detecting delamination damage in composites [17]. Hudson et al. fuse the merits of an air-coupled transducer and a scanning LDV to develop a fully non-contact system for inspecting local voids in composites [1]. Yu and Tian used a scanning LDV to acquire Lamb waves' time-space wavefields that could be processed by the short-space two-dimensional Fourier transform to analyze wavenumber changes and detect cracks [3]. With a hybrid system including a piezoelectric transducer to generate and a scanning LDV to acquire Lamb waves, Moll et al. constructed a high density circular array for detecting cracks with different orientations in an aluminum plate [21]. Jeon et al. proposed a compressive sensing-based high-speed full-field laser scanning approach that could effectively reduce the number of required laser scanning points in the structural inspection area [22]. Radzieński et al. showed the promise of hybrid systems that integrated piezoelectric transducers and a scanning LDV for identifying damages in different types of composite plates [24]. Ullah et al. recognized the limitations of piezoelectric transducer-LDV approaches in full wavefield acquisition and proposed a deep learning-based super-resolution method to enhance the efficiency of scanning LDV-based wavefield acquisition [25]. Despite these recent studies on laser technologies for generating and/or sensing elastic waves for various applications, there are very few studies on laser technologies for acquiring time-space wavefields of shear waves in viscoelastic materials, characterizing viscoelastic shear wave dispersion, and measuring the spatial distributions of viscoelastic properties such as shear elasticity $\mu_1$ and shear viscosity $\mu_2$.

Shear wave-based imaging is critical for both nondestructive evaluation and biomedical

applications, for example, the diagnosis of breast cancer [28], skin disease [29], hepatic fibrosis [30], and various pathologic and traumatic conditions of musculoskeletal soft tissues such as muscles, tendons, and ligaments [31,32]. Traditional shear wave-based imaging methods consider shear waves as a non-dispersive mode and use the measured shear wave speed at one frequency to evaluate the shear elasticity [33,34]. However, for viscoelastic materials such as soft tissues and biomimetic gelatin phantoms, previous studies found that shear waves should be considered as a dispersive mode whose wave speed changes with frequency [35–37]. This dispersive feature is in fact related to the material's shear viscosity that is usually neglected in traditional shear wave-based imaging methods [38–41]. In recent years, to measure the shear wave dispersion relation, most studies performed time-consuming measurements of wave traveling times at multiple frequencies and then calculate the shear wave velocities corresponding to those frequencies [37,42]. Few studies leverage methods based on time-space wavefield acquisition and analysis, which have the potential to quickly characterize the shear wave dispersion relation. Actually, time-space wavefields of waves can provide more information beyond the dispersion relation, such as revealing the propagation of dispersive modes and the wave interactions with material boundaries and internal damages [15]. In recent years, various wavefield analysis methods based on wavefield energy, multi-dimensional Fourier transform, wavefield correlation, and local wavenumber characterization have been developed [2,15,43]. Most studies focus on developing wavefield analysis methods to evaluate material damages such as cracks, corrosion, and delamination [11,12,17]. There are limited studies on developing methods to analyze time-space wavefields of shear waves in viscoelastic materials and characterize the spatial distributions of viscoelastic material properties.

To perform shear wave-based characterization of viscoelastic materials, the successful generation of shear waves is critical. The acoustic radiation force (ARF)-based methods, which

use the ARFs of high-energy ultrasonic beams generated by focused ultrasonic transducers or ultrasonic phased array transducers [35,44,45], are commonly used. These methods typically need large contact areas with test samples to generate strong shear waves, thus limiting their applications to small samples [39]. Moreover, their transducers usually have high costs, and the systems to drive and control the transducers are more costly. Another category of commonly used methods is based on shakers [46,47], which are bulky, difficult to use for portable applications, difficult to precisely control the output displacement, and difficult to integrate with shear wave sensors. We believe that new shear wave generation methods, which address the aforementioned limitations and have low-cost, compact, and low-power features, will greatly benefit the biomedical research community and accelerate the development of future shear wave-based imaging and viscoelastic material characterization techniques.

This study presents a piezo stack-LDV sensing approach, which leverages a low-cost, compact, low-power piezo stack to generate shear waves in viscoelastic materials, as well as an LDV integrated on a linear motion stage to acquire shear wave time-space wavefields. This study also presents wavefield analysis methods for analyzing the shear wave time-space wavefield, extracting the shear wave dispersion relation from the wavefield, obtaining local wavenumber distributions, and characterizing the spatial distributions of viscoelastic properties such as shear elasticity $\mu_1$ and shear viscosity $\mu_2$. To assist the wavefield analysis method development, a transfer function-based analytical model is formulated to simulate the propagation of dispersive shear waves, and the simulated time-space wavefields for different viscoelastic properties are used as the inputs to test wavefield analysis methods. To demonstrate the piezo stack-LDV system and wavefield analysis methods, proof-of-concept experiments were performed using a synthetic gelatin phantom. The results show that our piezo stack-LDV system can successfully generate shear waves and acquire time-space wavefields. Moreover, the wavefield analysis methods can analyze the acquired wavefields to reveal the

shear wave dispersion relation, show the spatial distributions of local wavenumbers, and characterize the spatial distributions of local viscoelastic properties such as shear elasticity $\mu_1$ and shear viscosity $\mu_2$. The remainder of this paper is organized as follows. Section 2 presents the design and mechanism of the piezo stack - LDV shear wave generation and sensing system. Section 3 presents the methods to analyze shear wave time-space wavefields and characterize shear wave dispersion, local wavenumber distributions, and local viscoelastic material property distributions. Section 4 presents a transfer function-based analytical model that can quickly simulate shear wave propagation in viscoelastic materials. Section 5 presents experimental studies to demonstrate our piezo stack - LDV system and wavefield processing methods by generating, acquiring, and analyzing shear waves in a synthetic gelation phantom. Section 6 concludes our study with key findings, discussion, and future work.

## 2. Piezo stack - LDV shear wave sensing system for acquiring shear wave time-space wavefields

Figure 1a shows a schematic of the piezo stack-LDV shear wave sensing system, which is composed of two key modules: a piezo stack-based shear wave generation module and a time-space wavefield acquisition module based on an LDV installed on a linear motion stage. The piezo stack is installed on a customized 3D fixture that can adjust the piezo stack's position and push the piezo stack against the test sample (*e.g.*, a viscoelastic gelatin phantom). In order to achieve better contact between the piezo stack and the test sample, a customized hemispherical head is attached to the end of the piezo stack. For shear wave generation, an excitation signal (*e.g.*, wideband chirp signal) is generated from an arbitrary function generator, amplified by a voltage amplifier, and then sent to the piezo stack actuator to output vertical displacement pulses from the tip of the piezo stack. The vertical displacement pulses can further excite shear waves propagating in the viscoelastic test sample. For shear wave acquisition, our system leverages an LDV installed on a linear motion stage, and the laser beam is set to an

orientation that is normal to the surface of the test sample to acquire the out-of-plane displacements of waves propagating in the sample based on the Doppler effect. The reason for using a normal-direction laser is that the shear waves generated by the piezo stack excitation method are mainly the shear vertical mode whose wave displacements are in the thickness direction.

To acquire time-space wavefields of shear waves, the aforementioned shear wave excitation and acquisition modules are synchronized and controlled by customized MATLAB codes. Through pitch-catch sensing with our piezo stack-LDV system, a waveform can be acquired, for example, $u(t, x_1)$ acquired with the laser spot set at a position $x_1$. After changing the laser spot position to $x_2$ and $x_n$, waveforms denoted as $u(t, x_1)$ and $u(t, x_n)$ can be acquired, as illustrated in Figure 1b. Therefore, through point-by-point measurements at a series of equally-spaced points along a user-defined scanning line (Figure 1a), the piezo stack - LDV system can acquire a series of waveforms. The combination of these waveforms results in a time-space wavefield $u(t, x)$, which can be considered as a wave displacement field function with respect to time $t$ and position $x$, as illustrated in Figure 1c. In order to correctly obtain key features (such as frequency and wavenumber) of shear waves, the Shannon sampling theorem should be followed to set the temporal and spatial sample rates. The sampling frequency should be at least twice the maximum wave frequency, and the spatial sampling resolution should be smaller than half of the minimum wavelength.

## 3. Methods for analyzing shear wave time-space wavefields

The time-space wavefield contains a wealth of information for both analyzing the propagation of dispersive waves and characterizing material properties. This section presents three methods for analyzing the time-space wavefields of shear waves in viscoelastic materials. First, a frequency-wavenumber analysis method based on the multi-dimensional Fourier transform is presented to characterize the dispersion relation of shear waves. Second, a frequency-

wavenumber dispersion analysis method is presented for the characterization of viscoelastic material properties including shear elasticity $\mu_1$ and shear viscosity $\mu_2$. Third, a space-frequency-wavenumber method is presented for obtaining the spatial distribution of local wavenumbers, as well as characterizing the spatial distributions of local viscoelastic material properties. In addition, these analysis methods are tested using both simulation data in Section 4 and experimental data in Section 5.

### *3.1. Frequency-wavenumber analysis of shear wave time-space wavefields*

To obtain wave signatures such as frequency and wavenumber information, the shear wave time-space wavefield can be transformed to a representation in the frequency-wavenumber domain by using a multi-dimensional Fourier transform expressed as [48]

$$U(f,\mathbf{k}) = \int_{-\infty}^{\infty}\int_{-\infty}^{\infty} u(t,\mathbf{x})e^{-i(2\pi ft-\mathbf{k}\cdot\mathbf{x})}dtd\mathbf{x}, \quad (1)$$

where $\mathbf{x} = (x, y, z)$ is a position vector and $\mathbf{k} = (k_x, k_y, k_z)$ is a wavenumber vector. $U(f, \mathbf{k})$ is the resulting frequency-wavenumber representation (or spectrum) that is a function of wave frequency $f$ and wavenumber vector $\mathbf{k}$. For a time-space wavefield acquired through point-by-point LDV measurements along a straight line (illustrated in Figure 1a), the frequency-wavenumber spectrum $U(f, \mathbf{k})$ in Eq. (1) should be reduced to $U(f, k = k_x)$ and accordingly the transformation equation should be

$$U(f,k) = \int_{-\infty}^{\infty}\int_{-\infty}^{\infty} u(t,x)e^{-i(2\pi ft-kx)}dtdx. \quad (2)$$

As illustrated in Figure 2b, the spectrum $U(f, k)$ obtained through the multi-dimensional Fourier transform can reveal the frequency-wavenumber components that are contained in the time-space wavefield $u(t, x)$. In this manner, we are able to analyze the shear wave time-space wavefield acquired by the piezo stack-LDV system and obtain the frequency-wavenumber dispersion relation of shear waves.

### *3.2. Wave dispersion analysis for characterizing viscoelastic properties*

When considering the shear viscosity effect, the shear wave becomes dispersive, and its frequency-wavenumber dispersion relation depends on both the shear elasticity and shear viscosity. The theoretical dispersion relation can be obtained by solving the shear wave characteristic equation. For the completeness of this paper, the key steps to formulate the shear wave characteristic equation based on the Kelvin-Voigt viscoelastic model are presented here. As illustrated by the inset in Figure 3a, the Kelvin-Voigt viscoelastic model has a spring and a dashpot in parallel, for considering the effects of shear elasticity $\mu_1$ and shear viscosity $\mu_2$, respectively. This model's stress-strain relation can be expressed as $\tau = (\mu_1 - \mu_2\,\partial/\partial t)\varepsilon$, where $\tau$ is shear stress and $\varepsilon$ is shear strain that equals to the vertical displacement's partial derivative $\partial u_z/\partial x$ [49]. By introducing this stress-strain relation for the Kelvin-Voigt viscoelastic model to the equation of motion, the wave equation for shear waves in a viscoelastic material can be derived as

$$\mu_1 \frac{\partial^2 u_z}{\partial x^2} - \mu_2 \frac{\partial^3 u_z}{\partial x^2 \partial t} = \rho \frac{\partial^2 u_z}{\partial t^2}, \tag{3}$$

where $\rho$ is density. By substituting the general wave displacement relation $u_z = U_z(\omega)e^{i(\omega t - kx)}$ where $\omega$ is the angular frequency into Eq. (3), we can obtain

$$(-\mu_1 k^2 + i\omega\mu_2 k^2 + \rho\omega^2)U_z(\omega) = 0. \tag{4}$$

Because $U_z(\omega)$ is a nonzero term, the expression in the parathesis should be zero. By solving the characteristic equation, we can obtain the following frequency-wavenumber relation,

$$k = \sqrt{\frac{\rho\omega^2}{\mu_1 + i\omega\mu_2}} = \mathrm{Re}(k) - i\,\mathrm{Im}(k), \tag{5}$$

$$\text{with } \mathrm{Re}(k) = \sqrt{\frac{\rho\omega^2\left(\sqrt{\mu_1^2+\omega^2\mu_2^2}+\mu_1\right)}{2(\mu_1^2+\omega^2\mu_2^2)}} \text{ and } \mathrm{Im}(k) = \sqrt{\frac{\rho\omega^2\left(\sqrt{\mu_1^2+\omega^2\mu_2^2}-\mu_1\right)}{2(\mu_1^2+\omega^2\mu_2^2)}},$$

where Re($k$) and Im($k$) are the real and imaginary parts of the wavenumber $k$, respectively. With the solved wavenumber, we can further derive the shear wave velocity $C_T = \omega/\mathrm{Re(k)}$ and

attenuation $\alpha_T$ = Im(k). Based on the frequency-wavenumber relation in Eq. (5), MATLAB codes are developed to plot a series of frequency-wavenumber dispersion curves for different viscoelastic properties (*e.g.*, different combinations of $\mu_1$ and $\mu_2$), in order to investigate the effects of materials properties on dispersion curves. As shown in Figure 3, the wavenumbers at low frequencies are more sensitive to the change of shear elasticity $\mu_1$, while high-frequency wavenumbers are more sensitive to the change of shear viscosity $\mu_2$. Moreover, with the decrease of shear viscosity $\mu_2$, the curved dispersion relation gradually changes to a straight line. Furthermore, as shown in Figure 3b, a 2D representation showing the wavenumber versus $\mu_1$ and $\mu_2$ at a selected frequency of 400 Hz, the wavenumber becomes larger with the decrease of either $\mu_1$ or $\mu_2$.

With the theoretical shear wave frequency-wavenumber dispersion curves corresponding to different material properties, we can compare these curves to the experimentally acquired frequency-wavenumber spectrum. Through comparison, the theoretical shear wave dispersion curve that best matches the spectrum data can be found, as illustrated in Figure 2c. The material properties used for calculating the best-match theoretical dispersion curve are considered as the measured viscoelastic properties of the test sample. To perform dispersion curve comparison for material property characterization, first, a database denoted as $\{k(f \mid \mu_1, \mu_2)\}$ is established by combining a collection of theoretical dispersion curves $k(f)$ for different combinations of $\mu_1$ and $\mu_2$. Second, from the experimental frequency-wavenumber spectrum, the wavenumbers $k_{\text{exp}}(f_i)$ that have maximum spectrum amplitudes for different frequencies $f_i$ ($i$ = 1, 2, 3… $N$) are identified, as illustrated by '+' markers in Figure 2b. Third, a least square method is used to search the database $\{k(f \mid \mu_1, \mu_2)\}$, in order to find the theoretical dispersion curve $k^{\text{opt}}(f)$ that best matches the experimental data $k_{\text{exp}}(f_i)$, as well as the shear elasticity $\mu_1^{\text{opt}}$ and shear viscosity $\mu_2^{\text{opt}}$ corresponding to the best-match theoretical dispersion curve. The dispersion curve comparison process can be expressed as

$$\mu_1^{\text{opt}}, \mu_2^{\text{opt}} = \arg\min_{\mu_1,\mu_2} \sum_{i=1}^{N} \left[ k_{\exp}(f_i) - k(f_i \mid \mu_1, \mu_2) \right]^2 . \quad (6)$$

Therefore, by analyzing the shear wave's dispersion relation using the aforementioned method, we can characterize a viscoelastic material's shear elasticity and shear viscosity. Note that the properties obtained by the aforementioned method are averaged values for the region where the time-space wavefield $u(t, x)$ is acquired.

### 3.3. Space-frequency-wavenumber characterization of spatial distributions of local viscoelastic material properties

The frequency-wavenumber analysis in Section 3.1. transforms a time-space wavefield to a frequency-wavenumber spectrum; however, the obtained frequency-wavenumber spectrum doesn't clearly provide spatial information. The dispersion analysis in Section 3.2 provides an approach to characterize viscoelastic material properties; however, this method doesn't carry the spatial information to characterize the spatial distributions of material properties. To overcome these limitations, we performed space-frequency-wavenumber analysis based on short-space Fourier transform, as illustrated in Figure 4. This analysis can retain the spatial information for characterizing the frequency-wavenumber relations at different positions (see Figure 4b) and the spatial distributions of material properties (see Figure 4d). In this method, the short-space Fourier transform [15] is applied to the acquired time-space wavefield $u(t, x)$ to obtain a space-frequency-wavenumber representation $S(\bar{x}, f, k)$ as:

$$S(\bar{x}, f, k) = \int_{-\infty}^{\infty} \int_{-\infty}^{\infty} u(t,x) W(x-\bar{x}) e^{-i(2\pi ft - kx)} dt dx , \quad (7)$$

where $W(x-\bar{x})$ is a short-space window centered at $\bar{x}$. In this study, the short-space window is formulated based on a Hanning function expressed as:

$$W(x-\bar{x}) = \begin{cases} \frac{1}{2}\left[ 1 + \cos\left( 2\pi \frac{|x-\bar{x}|}{D_x} \right) \right] & \text{if } |x-\bar{x}| \le D_x/2 \\ 0 & \text{otherwise} \end{cases} , \quad (8)$$

where $D_x$ is the window size that determines the spatial and wavenumber resolutions of the short-space Fourier transform. A larger window size $D_x$ leads to a higher wavenumber resolution while a lower spatial resolution. For this study, the window size $D_x$ is greater than two times of the wavelength of the used shear waves, to have a good wavenumber resolution.

The short-space Fourier transform method can be better explained through Figure 4a and 4b. As shown in Figure 4a, by multiplying a short-space window $W(x-\bar{x}_n)$ centered at $\bar{x}_n$, a windowed time-space wavefield $u(t,x)W(x-\bar{x}_n)$ can be obtained. By gradually moving the short-space window, the original time-space wavefield $u(t,x)$ can be discretized into a series of short-space time-space wavefields $\{u(t,x)W(x-\bar{x}_n)\}_N$ with center positions at $\{\bar{x}_n\}_N$ where $n = 1, 2, 3, \cdots, N$. By further applying multi-dimensional Fourier transform to all the discretized short-space time-space wavefields, a series of frequency-wavenumber spectra $\{U_n(f, k)\}_N$ (see Figure 4b) corresponding to windowed wavefields with different center positions $\{\bar{x}_n\}_N$ can be obtained. The collection of all the resulting frequency-wavenumber spectra can be represented using a space-frequency-wavenumber function $S(\bar{x}, f, k)$ in Eq. (7).

The obtained space-frequency-wavenumber representation $S(\bar{x}, f, k)$ can be used to analyze the changes of wave features and material properties with respect to position $\bar{x}$. As illustrated in Figure 4c, the space-wavenumber spectrum $S(\bar{x}, k)$ at a selected frequency of $f_m$ can show the changes of wavenumber components with respect to position $\bar{x}$. Moreover, by applying the material property characterization method in Section 3.2 to all the frequency-wavenumber spectra $\{U_n(f, k)\}_N$ (illustrated in Figure 4b) corresponding to different positions $\{\bar{x}_n\}_N$, we can obtain the spatial distributions of local viscoelastic properties such as the shear elasticity distribution $\{\mu_1(\bar{x}_n)\}_N$ (also denoted as $\mu_1(\bar{x})$) and the shear viscosity distribution $\{\mu_2(\bar{x}_n)\}_N$ (also denoted as $\mu_1(\bar{x})$), as illustrated in Figure 4d.

For shear waves in a small region, for example [$\bar{x}_n - D_x/2$, $\bar{x}_n + D_x/2$], the wave dispersion curve (*e.g.*, frequency-wavenumber curve) is an inherent wave property depending on the material properties in that small region and doesn't change with the incoming waves, such as waves already transmitted through other regions. In our method, we experimentally evaluate the frequency-wavenumber spectrum in that small section. Then, we obtain the theoretical frequency-wavenumber curve that best matches the experimental frequency-wavenumber spectrum. By using this approach, the obtained $\mu_1(\bar{x}_n)$ and $\mu_2(\bar{x}_n)$ are averaged material properties for the small, windowed region [$\bar{x}_n - D_x/2$, $\bar{x}_n + D_x/2$] where the experimental frequency-wavenumber spectrum is obtained.

## 4. Analytical modeling for simulating the time-space wavefields of dispersive shear waves in viscoelastic materials

In this Section, an analytical model is formulated by leveraging the shear wave dispersion relation, the transfer function method [50,51], and the Fourier transform. This method enables efficient simulations of dispersive shear waves that are generated by arbitrary time-domain displacement excitation. Based on the analytical model, time-space wavefields of shear waves in viscoelastic materials with different properties are simulated, and subsequently used as input wavefields to test the wavefield analysis methods presented in Section 3.

### *4.1. Analytical model of dispersive shear waves*

To simulate the propagation of dispersive shear waves in viscoelastic materials, numerical methods such as finite element and finite difference methods typically need long computation times and large computer memories [36,41,52]. To quickly simulate the propagation of dispersive shear waves generated by an arbitrary time-domain excitation signal, an analytical model is presented. The diagram in Figure 5 shows the key steps to establish the analytical model. First, an arbitrary time-domain excitation $u_e(t)$ is changed to a frequency-domain spectrum $U_e(\omega)$ through the Fourier transform. Second, the shear wave dispersion relation $k(\omega)$

is used to construct a transfer function $G(\omega, x)=e^{-ik(\omega)x}$. The transfer function here is for plane waves and the energy spreading effect that depends on the distance to the source is not considered [50,51]. Third, by multiplying the transfer function with the excitation spectrum $U_e(\omega)$, we can obtain a frequency-space function $U(\omega, x)$ that can be changed to a time-space wavefield $u(t, x)$ through inverse Fourier transform. Mathematically, the simulation model can be formulated as

$$u(t,x)=\mathcal{F}^{-1}\left[G(\omega,x)\cdot U_e(\omega)\right]=\mathcal{F}^{-1}\left[e^{-ik(\omega)x}\cdot\mathcal{F}[u_e(t)]\right], \tag{9}$$

where $\mathcal{F}[\cdot]$ and $\mathcal{F}^{-1}[\cdot]$ represent Fourier and inverse Fourier transforms that change data between time and frequency domains. Note that Eq. (9) for plane waves is sufficient to capture the wave dispersion effect, as it considers the frequency-dependent wavenumber $k(\omega)$. For cylindrical and spherical waves, distance-dependent terms $|x|^{-0.5}$ and $|x|^{-1}$ can be introduced to Eq. (9), respectively, for considering the energy spreading effects.

### *4.2. Simulation and analysis of shear wave time-space wavefields*

The analytical model in Eq.(9) is used to simulate shear waves generated by a chirp excitation modulated by a Tukey window that ensures smooth transitions at the beginning (or leading edge) and end (or trailing edge) of the chirp signal. As shown in Figure 6a, the input signal has a leading edge with gradually increasing amplitudes, a wide center part with an amplitude of 1, and a trailing edge with gradually decreasing amplitudes. The input signal's frequency spectrum is given in Figure 6b showing a wide frequency band from 0.3 to 1.8 kHz and a nearly flat top from 0.6 to 1.6 kHz. By using the analytical simulation method, we simulated dispersive shear waves in viscoelastic materials with different properties. By using the analytical simulation method, we simulated dispersive shear waves in viscoelastic materials with different properties, and the imaginary wavenumber Im($k$) related wave attenuation is not considered in these simulations. Figure 6c to 6e show the simulated time-space wavefields for three cases with ($\mu_1$ = 25 kPa, $\mu_2$ = 5 Pa·s), ($\mu_1$ = 50 kPa, $\mu_2$ = 5 Pa·s), and ($\mu_1$ = 50 kPa, $\mu_2$ = 10 Pa·s),

respectively, while the same density $\rho$ = 850 kg/m$^3$ is used. In the simulation results, as the waves propagate away from the source, the wave packet becomes more and more compact in the time domain. This is because of the wave dispersion effect with high-frequency waves propagating faster. Moreover, for different material properties, the wavefront slopes in the time-space wavefields are different, as different material properties lead to different shear wave speeds.

To test the wavefield analysis methods presented in Section 3, the simulated time-space wavefields are transformed to the frequency-wavenumber domain through the multi-dimensional Fourier transform. Figure 6f to 6h give the frequency-wavenumber spectra corresponding to the time-space wavefields in Figure 6c to 6e, respectively, and these spectra reveal the frequency-wavenumber dispersion relations contained in the shear wave time-space wavefields. In addition, we applied the dispersion analysis method established in Section 3.2 to the frequency-wavenumber spectra. The '+' markers in Figure 6f to 6h are identified wavenumber points with maximum spectrum amplitudes for different frequencies. The solid curves are the best-match frequency-wavenumber dispersion curves $k^{\mathrm{opt}}(f)$ that are obtained through the least square-based dispersion curve identification method in Section 3.2. In addition, the viscoelastic material properties $\mu_1^{\mathrm{opt}}$ and $\mu_2^{\mathrm{opt}}$, which are identified using Eq.(6), agree with the material properties used for analytical simulations. The results in Figure 6f to 6h prove the feasibility of our wavefield analysis methods for analyzing dispersive shear waves in viscoelastic materials with different properties.

## 5. Proof-of-concept experiments

Proof-of-concept experiments were performed to demonstrate a fully functional piezo stack-LDV system, as well as the wavefield analysis methods. Experiments were performed to demonstrate the piezo stack-based generation of shear waves in a viscoelastic material and the LDV-based acquisition of shear wave time-space wavefields. The acquired shear wave time-

space wavefields were analyzed to demonstrate the functions of wavefield analysis methods presented in Section 3, such as characterizing the shear wave dispersion relation using experimental data, characterizing viscoelastic material properties, and characterizing the spatial distributions of local properties such as wavenumber, shear elasticity, and shear viscosity.

### *5.1. Experimental setup and procedures*

Figure 7a shows a photo of the piezo stack-LDV experimental setup for generating shear waves in a viscoelastic phantom (180×120×30 mm) made of synthetic gelatin and acquiring time-space wavefields of the generated shear waves. As shown in Figure 7b, the shear wave actuator is composed of a 3×3×10 mm piezo stack (STEMINC, USA ) and a 3D-printed hemispherical head (radius 5 mm) attached to the tip of the piezo stack. The excitation signal for the piezo stack is generated from an arbitrary waveform function generator (Tektronix AFG3052C) and then amplified by a voltage amplifier (Krohn-Hite 7500). For this study, a 5-cycle sine wave modulated by a Hanning window is used as the excitation to generate narrow-band shear waves, and a chirp signal is used to generate wideband shear waves. Details of these excitation signals are given in Section 5.2 and 5.3.

To generate shear waves in a viscoelastic phantom, the piezo stack actuator is installed on a customized height-adjustable fixture and makes contact with the top surface of the viscoelastic phantom, as shown Figure 7b. Using this setup, the output thickness-direction displacement oscillation from the actuator can excite shear waves in the viscoelastic phantom. To acquire the generated shear waves, an LDV (Polytec OFV-505) installed on a customized 3D linear motion stage is used. The laser beam is normal to the phantom's top surface to measure the out-of-plane displacement waveforms of shear waves. The 3D linear motion stage is controlled by a motion controller and a customized MATLAB program to move the laser head to different locations for signal acquisition. Through point-by-point acquisition using a

piezo stack-LDV system illustrated in Figure 1a, we can acquire the generated shear waves at multiple points along a straight line and provide the time-space wavefield that can show the propagation of shear waves. For our experiments, the coordinate origin is at the piezo stack's center, and the scanning line is along the *x* axis, as illustrated by the sensing layout in Figure 7c. The spatial sampling resolution is set to 0.2 mm, and the sampling frequency is set to 65 kHz.

### *5.2. LDV scanning results and shear wave velocity measurement*

We used a narrow-band excitation signal with a center frequency of 400 Hz, to generate 400 Hz shear waves. Figure 8a and 8b show the waveform and frequency spectrum of the excitation signal. Figure 8c shows the acquired time-space wavefield of shear waves in the gelatin phantom. This wavefield can be considered as a collection of waveforms acquired at different locations. By using the distance to the wave source and the traveling time, the shear wave velocity can be measured. First, we used MATLAB codes to automatically identify valley positions from the time-space wavefield, and these valley positions were divided into four groups as illustrated in Figure 8c. Second, for each group of valley points, we can calculate the time difference $\Delta t_{n-1}$ using waveforms measured at $1^{st}$ and $n^{th}$ sampling points, as illustrated in Figure 8d. Third, using the time difference $\Delta t_{n-1}$ and the distance $\Delta x_{n-1}$ between two points, the shear wave velocity can be calculated by $C_T = \Delta x_{n-1} / \Delta t_{n-1}$. Fourth, this process is repeated for all the identified valley points in Figure 8c. Last, we perform a statistical analysis of the wave velocities calculated using all the valley points. The analysis result is given in Figure 8e. The obtained mean velocities for groups 1 to 4 are 7.653 m/s, 7.626 m/s, 7.675 m/s, and 7.636 m/s, respectively. The averaged velocity and standard deviation considering all the data groups are 7.648 m/s and 0.106 m/s. The obtained shear wave velocity falls in the velocity range (1 m/s to 15 m/s) found in literature [35,36,53,54]. From the statistical result in Figure 8e, it can also be seen that the extreme data points (indicated by the whiskers above and below the blue boxes) only have small deviations from the mean velocity.

### *5.3. Wavefield analysis results*

To generate shear waves in a wide frequency band, a Tukey window-modulated chip signal is generated by a function generator (Tektronix AFG3052C) and then amplified by a voltage amplifier (Krohn-Hite 7500). Figure 9a and 9b show a waveform and a spectrum of the measured excitation signal applied to the piezo stack actuator. It can be seen that the applied chirp excitation signal has amplitudes around 80 Vpp and covers frequencies from 0.3 to 1.8 kHz. Note that the gradual amplitude decrease from 5 to 20 ms is induced by the frequency-dependent amplification performance of the amplifier. The acquired time-space wavefield in Figure 9c is analyzed by using the wavefield field analysis methods presented in Section 3. Figure 9d shows a 2D spectrum obtained by using the frequency-wavenumber analysis method in Section 3.1, and this spectrum shows the frequency-wavenumber components of the generated shear waves. Because of the usage of a wideband chirp excitation, the frequency-wavenumber components in a wide frequency range are generated.

The wave dispersion analysis method established in Section 3.2 is applied to the frequency-wavenumber spectrum. First, for different frequencies, wavenumbers with the highest spectrum amplitudes are identified from the frequency-wavenumber spectrum. Second, by comparing these frequency-wavenumber points (marked with 'x' in Figure 9d) with a database of theoretical frequency-wavenumber dispersion curves, the dispersion curve (solid curve in Figure 9d) that best matches the experimental data is obtained. The viscoelastic material properties corresponding to the best-match dispersion curve are shear elasticity $\mu_1$ of 41 kPa and shear viscosity $\mu_2$ of 6 Pa·s. These values fall in the ranges 0.5-100 kPa and 0.75-9 Pa·s found in the literature [35,53–58]. For comparison, rheometers (HR20 and RSA-G2, TA Instruments) were used to perform rheological harmonic shear tests on three samples at 25 ℃. The average shear elasticity is 39.2 kPa. With the rheometry viscosity data and the power-law model for viscous materials [59,60], we obtained the average shear viscosity of 6.6 Pa·s for the

frequency range 0.3 to 1.8 kHz. Compared to the rheometry data, properties measured by our wave dispersion analysis approach have discrepancies of 4.6% for shear elasticity and 9.1% for shear viscosity.

The space-frequency-wavenumber analysis method presented in Section 3.3 is applied to the acquired time-space wavefield. Figure 10a shows the resulting space-wavenumber spectrum at a frequency of 400 Hz, and this result shows the wavenumber distribution versus location. By applying the dispersion analysis method in Eq.(6) to frequency-wavenumber spectra $\{U_n(f, k)\}_N$ corresponding to different positions $\{\bar{x}_n\}_N$, the spatial distributions of local viscoelastic properties such as the shear elasticity distribution and the shear viscosity distribution are obtained, as shown in Figure 10b. For the used uniform viscoelastic phantom, the results including wavenumber, shear elasticity, and shear viscosity almost have no changes. In our future study, we will further test the space-frequency-wavenumber method by using a nonuniform phantom with material property changes.

## 6. Conclusion and discussion

We have developed and demonstrated a piezo stack-LDV shear wave sensing system, which can generate narrow-band and wideband shear waves in viscoelastic materials by using a small piezo stack and can acquire time-space wavefields of the generated shear waves in a contactless and high-resolution manner based on an LDV integrated with a linear motion stage. The acquired time-space wavefields contain abundant information to obtain shear wave features such as velocity, frequency-wavenumber components, and wave dispersion. To analyze the wavefields of dispersive shear waves, this study presents multiple analysis methods including multi-dimensional Fourier transform-based frequency-wavenumber analysis, dispersion analysis-based material property characterization, and space-frequency-wavenumber analysis. These methods offer useful functions such as analysis of the frequency-wavenumber contents of the generated shear waves, characterization of the shear wave dispersion, extraction of

viscoelastic material properties (shear elasticity $\mu_1$ and shear viscosity $\mu_2$), and characterization of the spatial distributions of local wavenumbers and viscoelastic properties.

In addition to developing the piezo stack-LDV shear wave sensing method, we formulated an analytical model based on the dispersion curve solved from the wave characteristic equation that considers the Kelvin–Voigt viscoelastic model. Based on the analytical model, we simulated and compared time-space wavefields of wideband shear waves in viscoelastic materials with different properties. Our results show that the wave packet of wideband shear waves becomes more and more compact in the time domain. This is because of the frequency-dependent shear wave velocity, *i.e.*, the wave dispersion effect. Our parametric study shows that shear waves at high frequencies are more sensitive to the shear viscosity change and the low-frequency shear waves are more sensitive to the shear elasticity change. Using the simulated time-space wavefields as inputs, we also successfully tested our wavefield analysis methods.

For the proof-of-concept, a fully functional piezo stack-LDV sensing system was demonstrated by generating shear waves in a synthetic gelatin phantom and acquiring time-space wavefields in a noncontact and high-resolution manner. The measurement results prove that our piezo stack-LDV system can acquire the wavefields of narrow-band shear waves generated with a 5-count sine wave excitation and wideband shear waves generated with a chirp excitation. With the narrow-band time-space wavefield, we were able to obtain the shear wave velocity using the propagation distance and time. Moreover, by applying the frequency-wavenumber analysis and wave dispersion analysis methods to the wideband time-space wavefield, we were able to analyze the frequency-wavenumber components, characterize the shear wave dispersion relation, as well as characterize the viscoelastic material properties of our fabricated synthetic gelatin phantom. Moreover, by applying the space-frequency-wavenumber analysis method to the wideband time-space wavefield, we were able to

characterize the spatial distributions of local wavenumbers and local viscoelastic properties.

The experimental results prove the feasibility of our piezo stack-LDV sensing system and the presented methods for analyzing time-space wavefields, viscosity-induced wave dispersion, and frequency-wavenumber spectra of dispersive shear waves. This study contributes to laser ultrasonic technologies, by establishing a laser-based approach and showing its functions of acquiring time-space wavefields of shear waves in viscoelastic materials, characterizing the viscosity-induced shear wave dispersion, and characterizing the spatial distributions of viscoelastic properties. This study also contributes to shear wave analysis methods, by introducing multiple wavefield-based methods and showing their functions of characterizing both shear wave properties and viscoelastic material properties. In addition, this study provides a novel piezo stack-based method for generating shear waves in viscoelastic materials. Compared to commonly used methods, including the bulky shaker-based methods and the ARF-based methods that require expensive focused ultrasonic systems or high-power ultrasonic phased array systems, the piezo stack-based method has low-cost, compact, and low-power features, its output displacements can be easily controlled, and it can be used as a portable shear wave generation device. We expect that this research can greatly benefit the NDE and biomedical research communities and accelerate the development of future shear wave-based technologies for characterizing viscoelastic materials.

We will continue to work on this piezo stack-LDV technology to address its limitations. First, our proof-of-concept experiment still needs to use a bulky function generator and an amplifier. To develop a fully functional portable shear wave excitation device, we will replace these modules with a portable excitation signal generation device that leverages Arduino-based excitation signal generation and customized electronic board (*e.g.*, L298N driver board) -based low-frequency signal amplification. Second, this work is limited to acquiring and analyzing shear waves propagating along a line. Later, we will perform LDV-based wavefield acquisition

on a 2D flat surface and a 3D curved surface and then extend the shear wave analysis methods to those cases. Third, this work uses a uniform phantom with no spatial changes of material properties. Later, we will test our method using phantoms with spatial changes of material properties and real tissues (such as skin, muscle, and liver) through collaboration with biomedical researchers.

## Acknowledgments

The authors acknowledge the help from Mr. Joseph Rich at Duke University in conducting rheometry tests. The authors also acknowledge the financial support from the National Institute of General Medical Sciences of the National Institutes of Health (7R01GM144417), the National Science Foundation (CMMI-2243771 and CMMI-2340016), the Nuclear Energy University Programs (DE-NE0009187), the National Aeronautics and Space Administration (MS-80NSSC22M0273), and the Federal Aviation Administration (FAA 12-C-AM-MSU).

## References


[1] T.B. Hudson, T.-H. Hou, B.W. Grimsley, F.-G. Yuan, Imaging of local porosity/voids using a fully non-contact air-coupled transducer and laser Doppler vibrometer system, Structural Health Monitoring 16 (2017) 164–173.

[2] J. Segers, S. Hedayatrasa, G. Poelman, W. Van Paepegem, M. Kersemans, Self-reference broadband local wavenumber estimation (SRB-LWE) for defect assessment in composites, Mechanical Systems and Signal Processing 163 (2022) 108142.

[3] L. Yu, Z. Tian, Lamb wave structural health monitoring using a hybrid PZT-laser vibrometer approach, Structural Health Monitoring 12 (2013) 469–483.

[4] F.-G. Yuan, Structural health monitoring (SHM) in aerospace structures, Woodhead Publishing, 2016.

[5] B. Park, H. Sohn, C.-M. Yeum, T.C. Truong, Laser ultrasonic imaging and damage detection for a rotating structure, Structural Health Monitoring 12 (2013) 494–506.

[6] T. Wandowski, P.H. Malinowski, W.M. Ostachowicz, Circular sensing networks for guided waves based structural health monitoring, Mechanical Systems and Signal Processing 66–67 (2016) 248–267.

[7] L. Li, L. Zhu, C. Ma, L. Lin, J. Yao, L. Wang, K. Maslov, R. Zhang, W. Chen, J. Shi, L.V. Wang, Single-impulse panoramic photoacoustic computed tomography of small-animal whole-body dynamics at high spatiotemporal resolution, Nature Biomedical Engineering 1 (2017) 1–11.

[8] R. Haupt, K. Thomenius, A. Samir, R. Gurjar, M. Johnson, J. Sickler, M. Jakovljevic, B. Boitnott, Noncontact laser ultrasound (NCLUS) path to operational medical system, in: 2022 IEEE International Ultrasonics Symposium (IUS), 2022: pp. 1–6.

[9] X. Zhang, J.R. Fincke, C.M. Wynn, M.R. Johnson, R.W. Haupt, B.W. Anthony, Full noncontact laser ultrasound: first human data, Light: Science & Applications 8 (2019) 119.

[10] L.V. Wang, J. Yao, A practical guide to photoacoustic tomography in the life sciences, Nature Methods 13 (2016) 627–638.

[11] Z. Tian, S. Howden, Z. Ma, W. Xiao, L. Yu, Pulsed laser-scanning laser Doppler vibrometer (PL-SLDV) phased arrays for damage detection in aluminum plates, Mechanical Systems and Signal Processing 121 (2019) 158–170.

[12] S. Sampath, H. Sohn, Non-contact microcrack detection via nonlinear Lamb wave mixing and laser line arrays, International Journal of Mechanical Sciences 237 (2023) 107769.

[13] R.E. Morales, K.J. Harke, J.W. Tringe, D.M. Stobbe, T.W. Murray, Real-time laser ultrasonic monitoring of laser-induced thermal processes, Scientific Reports 12 (2022) 9865.

[14] D.-M. Chen, W.D. Zhu, Investigation of three-dimensional vibration measurement by a single scanning laser Doppler vibrometer, Journal of Sound and Vibration 387 (2017) 36–52.

[15] Z. Tian, W. Xiao, Z. Ma, L. Yu, Dispersion curve regression – assisted wideband local wavenumber analysis for characterizing three-dimensional (3D) profile of hidden corrosion damage, Mechanical Systems and Signal Processing 150 (2021) 107347.

[16] C.-Y. Ni, J.-C. LV, Y.-Y. Zhang, H.-Y. He, X.-F. Xia, Z.-H. Shen, V. Gusev, Laser ultrasonic monitoring of reversible/irreversible modification of a real crack under photothermal loading, Structural Health Monitoring 20 (2021) 173–187.

[17] P. Kudela, T. Wandowski, P. Malinowski, W. Ostachowicz, Application of scanning laser Doppler vibrometry for delamination detection in composite structures, Optics and Lasers in Engineering 99 (2017) 46–57.

[18] S.J. Rothberg, M.S. Allen, P. Castellini, D. Di Maio, J.J.J. Dirckx, D.J. Ewins, B.J. Halkon, P. Muyshondt, N. Paone, T. Ryan, H. Steger, E.P. Tomasini, S. Vanlanduit, J.F. Vignola,

An international review of laser Doppler vibrometry: Making light work of vibration measurement, Optics and Lasers in Engineering 99 (2017) 11–22.
[19] W.J. Staszewski, B.C. Lee, R. Traynor, Fatigue crack detection in metallic structures with Lamb waves and 3D laser vibrometry, Measurement Science and Technology 18 (2007) 727.
[20] S. Majhi, A. Mukherjee, N.V. George, V. Karaganov, B. Uy, Corrosion monitoring in steel bars using Laser ultrasonic guided waves and advanced signal processing, Mechanical Systems and Signal Processing 149 (2021) 107176.
[21] J. Moll, L. De Marchi, C. Kexel, A. Marzani, High resolution defect imaging in guided waves inspections by dispersion compensation and nonlinear data fusion, Acta Acustica United with Acustica 103 (2017) 941–949.
[22] J.Y. Jeon, Y. Miao, G. Park, E. Flynn, Compressive laser scanning with full steady state wavefield for structural damage detection, Mechanical Systems and Signal Processing 169 (2022) 108626.
[23] Ł. Ambroziński, T. Stepinski, T. Uhl, Efficient tool for designing 2D phased arrays in lamb waves imaging of isotropic structures, Journal of Intelligent Material Systems and Structures 26 (2015) 2283–2294.
[24] M. Radzieński, P. Kudela, A. Marzani, L. De Marchi, W. Ostachowicz, Damage identification in various types of composite plates using guided waves excited by a piezoelectric transducer and measured by a laser vibrometer, Sensors 19 (2019) 1958.
[25] S. Ullah, P. Kudela, W. Ostachowicz, A deep learning based super-resolution approach for the reconstruction of full wavefields of Lamb waves, in: American Society of Mechanical Engineers Digital Collection, 2023.
[26] P. Rizzo, A. Enshaeian, Challenges in bridge health monitoring: a review, Sensors 21 (2021) 4336.
[27] R. Yang, S.K. Singh, M. Tavakkoli, N. Amiri, Y. Yang, M.A. Karami, R. Rai, CNN-LSTM deep learning architecture for computer vision-based modal frequency detection, Mechanical Systems and Signal Processing 144 (2020) 106885.
[28] J.H. Youk, H.M. Gweon, E.J. Son, Shear-wave elastography in breast ultrasonography: the state of the art, Ultrasonography 36 (2017) 300–309.
[29] S.-Y. Huang, X. Xiang, R.-Q. Guo, S. Cheng, L.-Y. Wang, L. Qiu, Quantitative assessment of treatment efficacy in keloids using high-frequency ultrasound and shear wave elastography: a preliminary study, Scientific Reports 10 (2020) 1375.
[30] E. Herrmann, V. de Lédinghen, C. Cassinotto, W.C.-W. Chu, V.Y.-F. Leung, G. Ferraioli, C. Filice, L. Castera, V. Vilgrain, M. Ronot, Assessment of biopsy-proven liver fibrosis by two-dimensional shear wave elastography: An individual patient data-based meta-analysis, Hepatology 67 (2018) 260–272.
[31] J. Blank, M. Blomquist, L. Arant, S. Cone, J. Roth, Characterizing musculoskeletal tissue mechanics based on shear wave propagation: a systematic review of current methods and reported measurements, Annals of Biomedical Engineering 50 (2022) 751–768.
[32] S.K. Crawford, D. Thelen, J.M. Yakey, B.C. Heiderscheit, J.J. Wilson, K.S. Lee, Regional shear wave elastography of Achilles tendinopathy in symptomatic versus contralateral Achilles tendons, European Radiology 33 (2023) 720–729.
[33] A.J. Engel, G.R. Bashford, A new method for shear wave speed estimation in shear wave elastography, IEEE Transactions on Ultrasonics, Ferroelectrics, and Frequency Control 62 (2015) 2106–2114.
[34] H. Zhao, P. Song, M.W. Urban, J.F. Greenleaf, S. Chen, Shear wave speed measurement using an unfocused ultrasound beam, Ultrasound in Medicine & Biology 38 (2012) 1646–1655.
[35] P. Kijanka, M.W. Urban, Local phase velocity based imaging of viscoelastic phantoms

and tissues, IEEE Transactions on Ultrasonics, Ferroelectrics, and Frequency Control 68 (2020) 389–405.
[36] F. Zvietcovich, N. Baddour, J.P. Rolland, K.J. Parker, Shear wave propagation in viscoelastic media: Validation of an approximate forward model, Physics in Medicine and Biology 64 (2019) 025008.
[37] N.C. Rouze, Y. Deng, C.A. Trutna, M.L. Palmeri, K.R. Nightingale, Characterization of viscoelastic materials using group shear wave speeds, IEEE Transactions on Ultrasonics, Ferroelectrics, and Frequency Control 65 (2018) 780–794.
[38] B. Zhou, X. Zhang, Comparison of five viscoelastic models for estimating viscoelastic parameters using ultrasound shear wave elastography, Journal of the Mechanical Behavior of Biomedical Materials 85 (2018) 109–116.
[39] E.G. Simon, S. Callé, F. Perrotin, J.-P. Remenieras, Measurement of shear wave speed dispersion in the placenta by transient elastography: A preliminary ex vivo study, PloS One 13 (2018) e0194309.
[40] J. Ormachea, K.J. Parker, Comprehensive viscoelastic characterization of tissues and the inter-relationship of shear wave (group and phase) velocity, attenuation and dispersion, Ultrasound in Medicine & Biology 46 (2020) 3448–3459.
[41] P. Kijanka, M.W. Urban, Phase Velocity Estimation with Expanded Bandwidth in Viscoelastic Phantoms and Tissues, IEEE Transactions on Medical Imaging 40 (2021) 1352.
[42] S. Chen, M.W. Urban, C. Pislaru, R. Kinnick, Y. Zheng, A. Yao, J.F. Greenleaf, Shearwave dispersion ultrasound vibrometry (SDUV) for measuring tissue elasticity and viscosity, IEEE Transactions on Ultrasonics, Ferroelectrics, and Frequency Control 56 (2009) 55–62.
[43] J. He, F.-G. Yuan, Damage identification for composite structures using a cross-correlation reverse-time migration technique, Structural Health Monitoring 14 (2015) 558–570.
[44] J.A. Martin, D.G. Schmitz, A.C. Ehlers, M.S. Allen, D.G. Thelen, Calibration of the shear wave speed-stress relationship in ex vivo tendons, Journal of Biomechanics 90 (2019) 9–15.
[45] J. Ormachea, K.J. Parker, Elastography imaging: the 30 year perspective, Phys. Med. Biol. 65 (2020) 24TR06.
[46] B. Zhou, X. Yang, X. Zhang, W.J. Curran, T. Liu, Ultrasound elastography for lung disease assessment, IEEE Transactions on Ultrasonics, Ferroelectrics, and Frequency Control 67 (2020) 2249–2257.
[47] C. Huang, P. Song, D.C. Mellema, P. Gong, U.-W. Lok, S. Tang, W. Ling, D.D. Meixner, M.W. Urban, A. Manduca, J.F. Greenleaf, S. Chen, Three-dimensional shear wave elastography on conventional ultrasound scanners with external vibration, Phys Med Biol 65 (2020) 215009.
[48] D.H. Johnson, D.E. Dudgeon, Array signal processing: concepts and techniques, Prentice Hall., 1993.
[49] S. Catheline, J.-L. Gennisson, G. Delon, M. Fink, R. Sinkus, S. Abouelkaram, J. Culioli, Measurement of viscoelastic properties of homogeneous soft solid using transient elastography: An inverse problem approach, The Journal of the Acoustical Society of America 116 (2004) 3734–3741.
[50] Y. Shen, V. Giurgiutiu, WaveFormRevealer: An analytical framework and predictive tool for the simulation of multi-modal guided wave propagation and interaction with damage, Structural Health Monitoring 13 (2014) 491–511.
[51] Victor. Giurgiutiu, Structural health monitoring with piezoelectric wafer active sensors, Elsevier/Academic Press, 2008.

[52] M.L. Palmeri, B. Qiang, S. Chen, M.W. Urban, Guidelines for Finite-Element Modeling of Acoustic Radiation Force-Induced Shear Wave Propagation in Tissue-Mimicking Media, IEEE Transactions on Ultrasonics, Ferroelectrics, and Frequency Control 64 (2017) 78–92.
[53] A.P. Sarvazyan, A.R. Skovoroda, S.Y. Emelianov, J.B. Fowlkes, J.G. Pipe, R.S. Adler, R.B. Buxton, P.L. Carson, Biophysical bases of elasticity imaging, in: J.P. Jones (Ed.), Acoustical Imaging, Springer US, Boston, MA, 1995: pp. 223–240.
[54] J.M. Pereira, J.M. Mansour, B.R. Davis, Analysis of shear wave propagation in skin; application to an experimental procedure, Journal of Biomechanics 23 (1990) 745–751.
[55] L.M. Wiseman, M.W. Urban, R.J. McGough, A parametric evaluation of shear wave speeds estimated with time-of-flight calculations in viscoelastic media, The Journal of the Acoustical Society of America 148 (2020) 1349.
[56] Y. Wang, M.F. Insana, Viscoelastic properties of rodent mammary tumors using ultrasonic shear-wave imaging, Ultrasonic Imaging 35 (2013) 126–145.
[57] A. Callejas, A. Gomez, I.H. Faris, J. Melchor, G. Rus, Kelvin–Voigt parameters reconstruction of cervical tissue-mimicking phantoms using torsional wave elastography, Sensors 19 (2019) 3281.
[58] K. Tachi, H. Hasegawa, H. Kanai, Measurement of shear viscoelasticity using dual acoustic radiation pressure induced by continuous-wave ultrasounds, Japanese Journal of Applied Physics 53 (2014) 07KF17.
[59] C.W. Macosko, Rheology: Principles, Measurements, and Applications, VCH, 1994.
[60] A. Bonfanti, J. L. Kaplan, G. Charras, A. Kabla, Fractional viscoelastic models for power-law materials, Soft Matter 16 (2020) 6002–6020.

## Figures

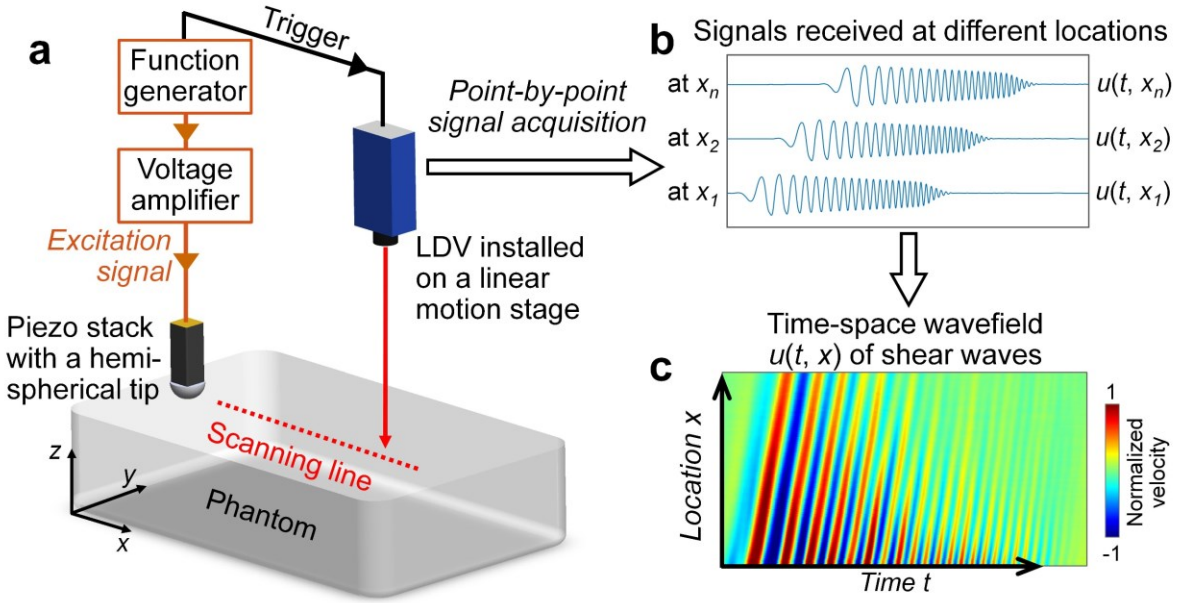


**Figure 1.** Illustration of the piezo stack - LDV shear wave sensing approach: **(a)** Schematic of the piezo stack - LDV sensing system that uses a piezo stack to generate shear waves and an LDV to acquire shear wave signals. **(b)** Example waveforms $u(t, x_n)$ acquired at different locations $x_n$ along a scanning line. **(c)** Example shear wave time-space wavefield $u(t, x)$ that can be acquired by our piezo stack - LDV sensing approach.

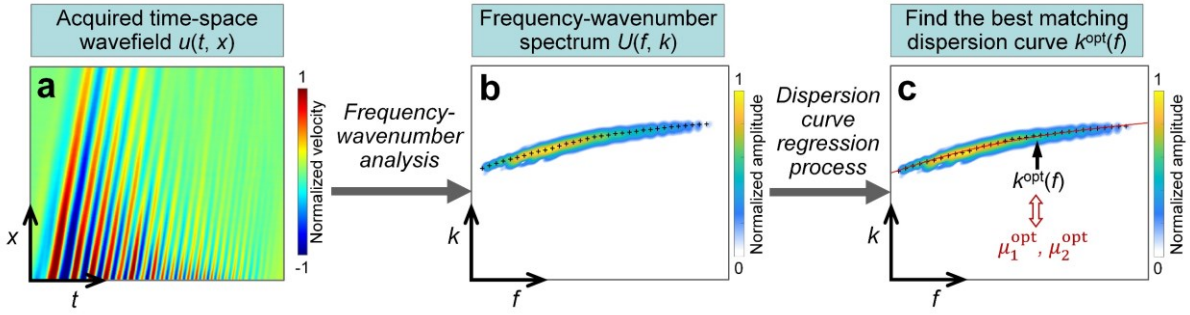


**Figure 2.** Illustration of the wavefield analysis method for determining the viscoelastic material properties. **(a** to **b)** A time-space wavefield $u(t, x)$ acquired by the piezo stack - LDV sensing system is transformed to a frequency-wavenumber spectrum $U(f, k)$, by using 2D Fourier transform. **(b** to **c)** The theoretical dispersion curve $k^{opt}(f)$ that best matches the experimental frequency-wavenumber spectrum $U(f, k)$ is selected, by using a process that compares the experimental spectrum with a database of theoretical dispersion curves that are precalculated for different viscoelastic material properties. The '+' markers in (b) indicate wavenumber points with maximum spectrum amplitudes for different frequencies. The shear elasticity and shear viscosity that are used to calculate the best matching theoretical dispersion curve $k^{opt}(f)$ are denoted as $\mu_1^{opt}$ and $\mu_2^{opt}$.

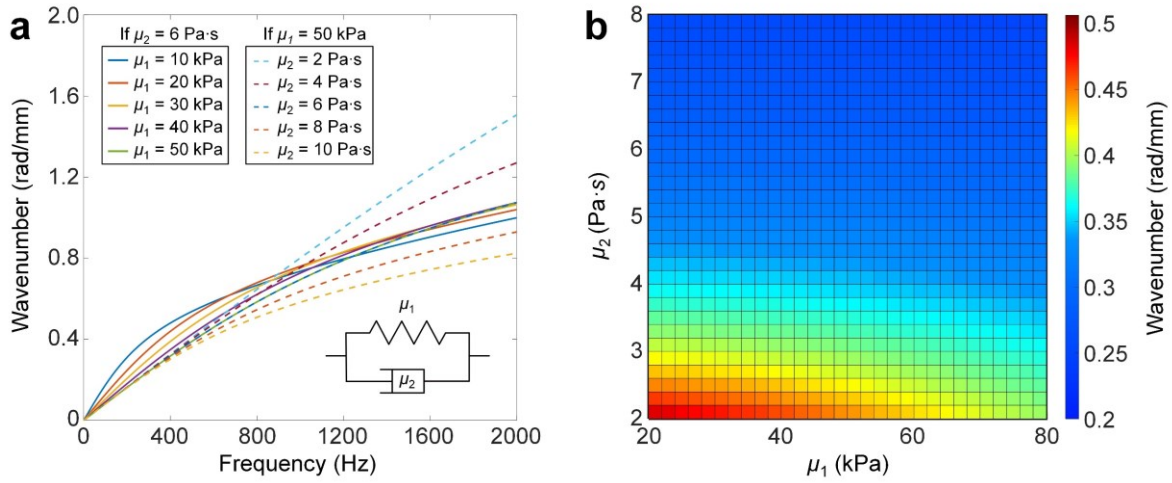


**Figure 3.** Theoretical shear wave dispersion relations derived based on the Kelvin–Voigt model. **(a)** A group of theoretical frequency-wavenumber dispersion curves for viscoelastic materials with different shear elasticities and shear viscosities. **(b)** Wavenumber variation versus shear elasticity $\mu_1$ and shear viscosity $\mu_2$ when the shear wave frequency is 400 Hz.

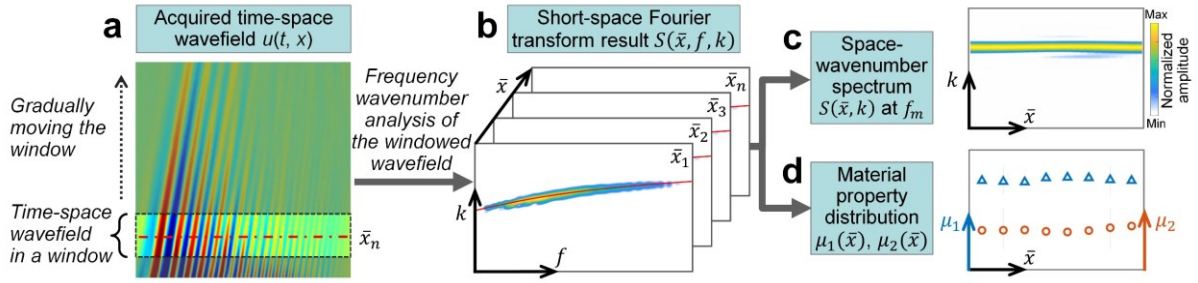


**Figure 4.** Illustrations of the short-space Fourier transform method and its application for characterizing material property distributions. **(a)** Schematic to illustrate the process of using a short-space window to isolate a windowed time-space wavefield. By gradually moving the short-space window's center position, the original time-space wavefield can be discretized into a series of short-space time-space wavefields whose center positions are at $\{\bar{x}_n\}_N$ where $n$ = 1, 2, 3, · · ·, $N$. **(b)** By applying 2D Fourier transform to all the discretized short-space time-space wavefields, a series of frequency-wavenumber spectra that correspond to windowed wavefields with different center positions $\{\bar{x}_n\}_N$ can be obtained. **(c)** Example of a space-wavenumber spectrum S($\bar{x}$, $k$) that can be obtained from the short-space Fourier transform result at a frequency of $f_m$. **(d)** Material property distributions $\mu_1(\bar{x})$ and $\mu_2(\bar{x})$ can be determined, by applying dispersion curve analysis to all the frequency-wavenumber relations of the short-space Fourier transform result in (b).

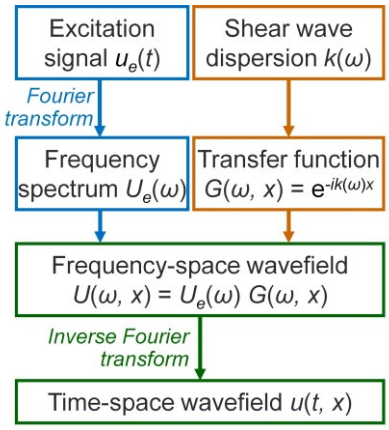


**Figure 5.** A diagram showing key steps for the analytical simulation of the shear wave time-space wavefield $u(t, x)$

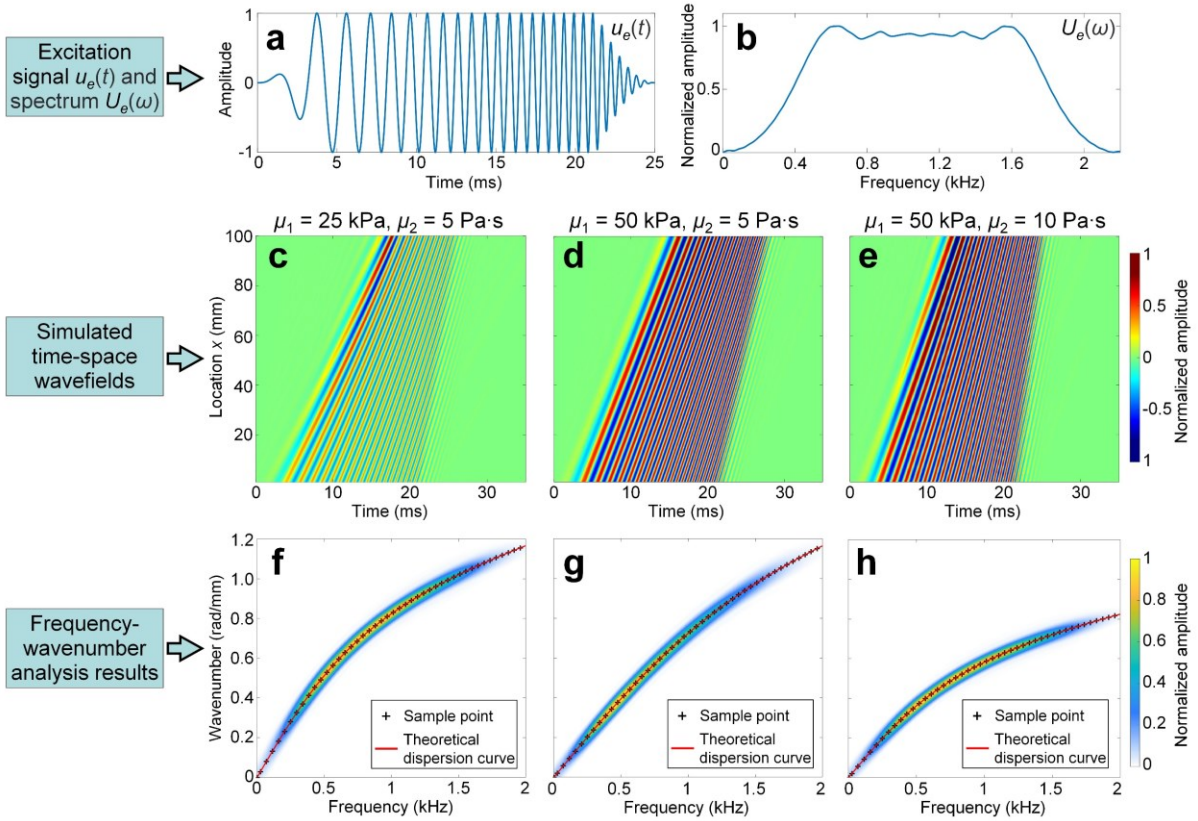


**Figure 6.** Analytical simulation results for cases with different material properties. **(a)** Time-domain waveform of a window chirp signal that is used as the excitation. **(b)** Frequency spectrum of the excitation waveform. **(c-e)** Simulated time-space wavefields for three cases with ($\mu_1$ = 25 kPa, $\mu_2$ = 5 Pa·s), ($\mu_1$ = 50 kPa, $\mu_2$ = 5 Pa·s), and ($\mu_1$ = 50 kPa, $\mu_2$ = 10 Pa·s), respectively. **(f-h)** Frequency wavenumber spectra corresponding to the time-space wavefields in (c) to (e), respectively.

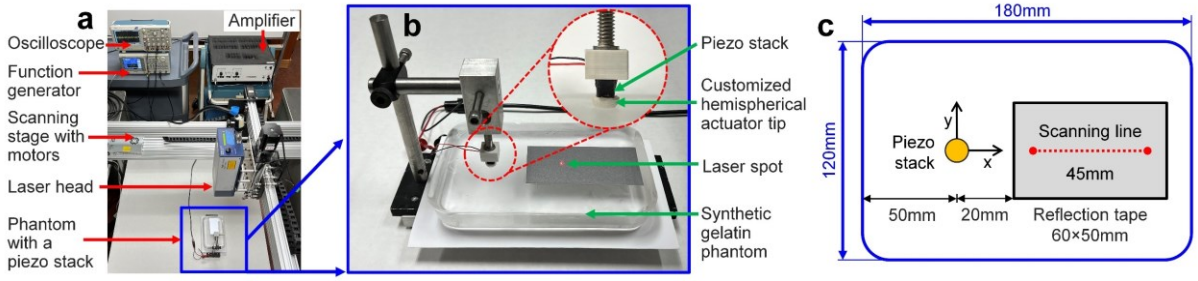


**Figure 7.** Experimental setup for characterizing the viscoelastic properties of a synthetic gelatin phantom. **(a)** Photo of the piezo stack - LDV shear wave sensing setup. **(b)** Close view of the test setup showing a small piezo stack with a customized hemispherical actuator tip, a laser spot, and a synthetic gelatin phantom. **(c)** A schematic showing the experimental sensing layout.

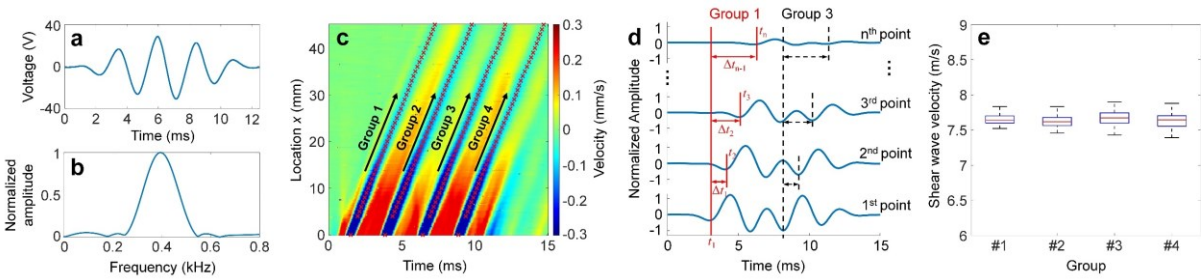


**Figure 8.** Experimental results acquired by the piezo stack - LDV shear wave sensing approach. **(a)** and **(b)** Waveform and frequency spectrum of the excitation signal (5-count 400 Hz sine wave modulated by a Hanning window) applied to the piezo stack. **(c)** An acquired time-space wavefield of shear waves. The red markers 'x' indicate the wave valley positions. **(d)** Schematic showing the approach used to measure traveling times of shear waves. Using the traveling time and propagation distance, we can further determine the shear wave velocity. **(e)** Experimentally measured shear wave velocities for four groups that correspond to the valleys marked in figure (c). The red line within each blue box indicates the median, the bottom and top edges of each box indicate the 25$^{th}$ and 75$^{th}$ percentiles, the whiskers extend to the extreme data points.

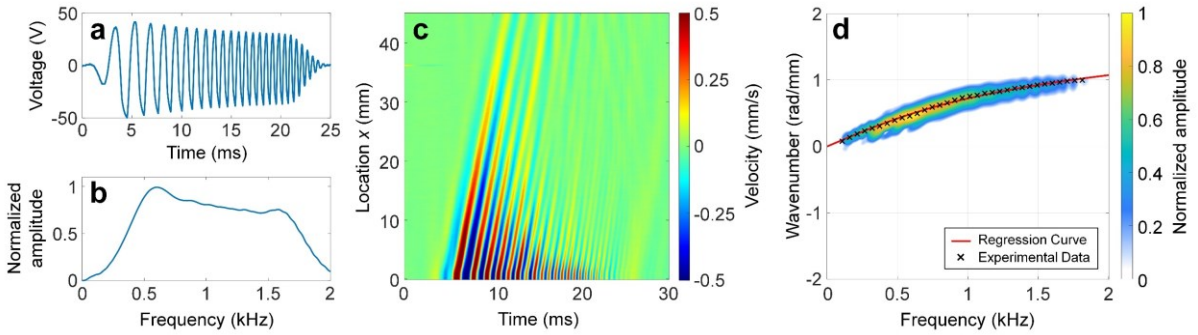


**Figure 9.** Frequency-wavenumber analysis results for wideband shear waves. **(a)** and **(b)** Waveform and frequency spectrum of a chirp excitation signal applied to the piezo stack. **(c)** An acquired time-space wavefield of shear waves generated by the piezo stack with a chirp excitation. **(d)** A frequency-wavenumber spectrum with obtained best-match dispersion curve. The markers 'x' indicates experimental data that are extracted from the frequency-wavenumber spectrum by finding the local spectrum maxima at different frequencies. The solid line represents the dispersion curve that best matches the experimental frequency-wavenumber data. The material properties used for calculating the best matching theoretical dispersion curve are $\mu_1$ of 41 kPa and $\mu_2$ of 6.0 Pa·s.

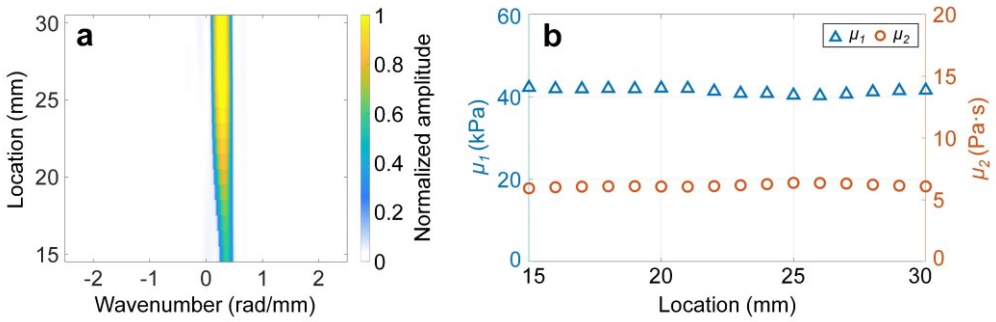


**Figure 10.** Short-space wavefield analysis results. **(a)** 2D image showing the obtained space-wavenumber spectrum at $f = 400$Hz. **(b)** Scatter plots showing the distributions of measured shear elasticity $\mu_1$ and shear viscosity $\mu_2$ versus location $x$.